






Article

Fibroblast Activation Protein-Targeting Minibody-IRDye700DX for Ablation of the Cancer-Associated Fibroblast with Photodynamic Therapy

Esther M. M. Smeets ^{1,†} , Daphne N. Dorst ^{2,†} , Gerben M. Franssen ¹, Merijn S. van Essen ¹, Cathelijne Frielink ¹, Martijn W. J. Stommel ³, Marija Trajkovic-Arsic ^{4,5}, Phyllis F. Cheung ^{4,5}, Jens T. Siveke ^{4,5} , Ian Wilson ⁶, Alessandro Mascioni ⁶, Erik H. J. G. Aarntzen ¹  and Sanne A. M. van Lith ^{1,*} 

¹ Department of Medical Imaging, Radboud University Medical Center, 6525 GA Nijmegen, The Netherlands; esther.markus-smeets@radboudumc.nl (E.M.M.S.)

² Department of Experimental Rheumatology, Radboud Institute for Molecular Life Sciences, 6525 GA Nijmegen, The Netherlands

³ Department of Surgery, Radboud University Medical Center, 6525 GA Nijmegen, The Netherlands

⁴ Bridge Institute of Experimental Tumour Therapy, West German Cancer Centre, University Hospital Essen, University of Duisburg-Essen, 47057 Essen, Germany

⁵ Division of Solid Tumour Translational Oncology, German Cancer Consortium (DKTK Partner Site Essen) and German Cancer Research Centre, DKFZ, 69120 Heidelberg, Germany

⁶ ImaginAb, Inglewood, CA 90301, USA

* Correspondence: sanne.vanlith@radboudumc.nl

† These authors contributed equally to this work.



Citation: Smeets, E.M.M.; Dorst, D.N.; Franssen, G.M.; van Essen, M.S.; Frielink, C.; Stommel, M.W.J.; Trajkovic-Arsic, M.; Cheung, P.F.; Siveke, J.T.; Wilson, I.; et al. Fibroblast Activation Protein-Targeting Minibody-IRDye700DX for Ablation of the Cancer-Associated Fibroblast with Photodynamic Therapy. *Cells* **2023**, *12*, 1420. <https://doi.org/10.3390/cells12101420>

Academic Editor: Kazuhito Satomura

Received: 22 March 2023

Revised: 4 May 2023

Accepted: 16 May 2023

Published: 18 May 2023



Copyright: © 2023 by the authors. Licensee MDPI, Basel, Switzerland. This article is an open access article distributed under the terms and conditions of the Creative Commons Attribution (CC BY) license (<https://creativecommons.org/licenses/by/4.0/>).

Abstract: Fibroblast activation protein (FAP), expressed on cancer-associated fibroblasts, is a target for diagnosis and therapy in multiple tumour types. Strategies to systemically deplete FAP-expressing cells show efficacy; however, these induce toxicities, as FAP-expressing cells are found in normal tissues. FAP-targeted photodynamic therapy offers a solution, as it acts only locally and upon activation. Here, a FAP-binding minibody was conjugated to the chelator diethylenetriaminepentaacetic acid (DTPA) and the photosensitizer IRDye700DX (DTPA-700DX-MB). DTPA-700DX-MB showed efficient binding to FAP-overexpressing 3T3 murine fibroblasts (3T3-FAP) and induced the protein's dose-dependent cytotoxicity upon light exposure. Biodistribution of DTPA-700DX-MB in mice carrying either subcutaneous or orthotopic tumours of murine pancreatic ductal adenocarcinoma cells (PDAC299) showed maximal tumour uptake of ¹¹¹In-labelled DTPA-700DX-MB at 24 h post injection. Co-injection with an excess DTPA-700DX-MB reduced uptake, and autoradiography correlated with FAP expression in the stromal tumour region. Finally, in vivo therapeutic efficacy was determined in two simultaneous subcutaneous PDAC299 tumours; only one was treated with 690 nm light. Upregulation of an apoptosis marker was only observed in the treated tumours. In conclusion, DTPA-700DX-MB binds to FAP-expressing cells and targets PDAC299 tumours in mice with good signal-to-background ratios. Furthermore, the induced apoptosis indicates the feasibility of targeted depletion of FAP-expressing cells with photodynamic therapy.

Keywords: minibody; targeted photodynamic therapy (tPDT); cancer-associated fibroblast (CAF); fibroblast activation protein (FAP); pancreatic ductal adenocarcinoma (PDAC)

1. Introduction

Fibroblast activation protein (FAP) is a type II integral serine protease that is expressed by activated fibroblasts. It facilitates remodelling of the extracellular matrix and therefore is involved in functions such as cell adhesion, invasion, and motility. In over 90% of epithelial tumours, FAP expression is found on the cancer-associated fibroblasts (CAFs). These cells have a critical role in promoting tumour growth, invasion, metastasis, and immunosuppression and ultimately in the clinical outcome of patients [1–5]. The development and

application of tracers for non-invasive imaging FAP-expressing cells have therefore gained widespread interest over the past years [6,7].

Besides imaging, targeted depletion of FAP-expressing cells is an appealing treatment option. Depletion of FAP-expressing cells was investigated in transgenic mice with FAP-promotor driven diphtheria toxin receptor (DTR) [5] or using pharmacological FAP inhibitors [8], FAP-targeting vaccines and T-cell therapies [9–12], and FAP-targeting molecules coupled to cytotoxic compounds [13–17]. These compounds inhibit tumour growth and induce anti-tumour immune responses in various preclinical models; however, some studies also describe severe systemic toxicity, including cachexia and anaemia [18,19]. This indicates the importance of FAP-expressing cells in maintaining normal muscle mass and haematopoiesis. Furthermore, it warrants caution, as FAP expression is also found in wound healing and normal tissues such as the placenta, uterine stroma, embryonic tissue, and multipotent bone marrow stromal cells [5,20,21].

Targeted photodynamic therapy offers a potential solution to these limitations. Here, a targeting compound conjugated to a photosensitizer is activated by light of a specific wavelength, inducing production of reactive oxygen species and resulting in cell death. As opposed to non-targeted photodynamic therapy using the photosensitizer alone, in this approach, off-target toxicity is avoided. Furthermore, as the photosensitizer conjugate is only activated in the region of interest, the effects of eliminating target-expressing cells in other tissues or organs are avoided. The silica-phthalocyanine derivative IRDye700DX is highly suitable and often used for targeted photodynamic therapy, as the water-soluble axial ligands increase hydrophilicity, and the NHS ester enables conjugation to targeting proteins such as antibodies. Furthermore, it is activated with near-infrared light (690 nm), is very photostable, and has a high singlet oxygen quantum yield [22–24].

We and others have proven the feasibility of FAP-targeted photodynamic therapy with a monoclonal antibody [25–31] or with nanoparticles [32,33]. Though high binding affinity and long circulation time often lead to high uptake of monoclonal antibodies at the target site, smaller molecules could lead to better tissue penetration. In addition, faster blood clearance could lead to a shorter time interval between injection and exposure to light. Other studies have shown similar or increased efficiency of photodynamic therapy with smaller molecules such as nanobodies (~15 kDa), diabodies (~45 kDa), or minibodies (~75 kDa) when compared to a monoclonal antibody [34,35]. Here, we optimized FAP-targeted photodynamic therapy with a minibody. These are comprised of antigen binding single-chain fragment variable regions fused to the C_H3 region of the human Fc domain. Minibodies maintain the specificity and avidity of full-length antibodies while being biologically inert and lacking immune effector functions. The use of minibodies in non-invasive imaging has shown successful in preclinical [36,37] and initial clinical results [38,39].

Here, we generated a minibody conjugated to the phthalocyanine-based photosensitizer IRDye700DX for application in photodynamic therapy and the chelator DTPA for ¹¹¹In-labeling and quantification or visualization of the tracer in biodistribution and imaging studies. We aim to provide proof of concept for the feasibility of FAP-targeted photodynamic therapy in FAP-expressing cell lines *in vitro* and in a syngeneic murine model carrying subcutaneous and orthotopic tumours of a murine pancreatic ductal adenocarcinoma (PDAC) cell line, as PDAC is a tumour type in which FAP-expressing CAFs play a large role.

2. Materials and Methods

2.1. Minibody Conjugation and Characterization

A minibody directed at binding human FAP was developed by ImaginAb Inc. (Inglewood, CA, USA). The minibody was conjugated to p-isothiocyanatobenzyl DTPA (ITC-DTPA, Macrocyclics, Plano, TX, USA) and N-Hydroxysuccinimide IRDye700DX (NHS-IRDye700DX, Licor, Lincoln, NE, USA). NHS-IRDye700DX was added in a 5-fold molar excess in 10% *v/v* NaHCO₃, pH 8.5, and incubated for 1 h, and then, ITC-DTPA was added in a 15-fold molar excess in 10% *v/v* NaHCO₃, pH 9.5, and incubated for 1 h at room

temperature. Conjugates were subsequently dialyzed in PBS (pH 7.4) with 1 g/L Chelex (Bio-Rad laboratories Inc., Hercules, CA, USA) to remove unconjugated probes. UV-visible absorbance spectra of 5 μ M NHS-IRDye700DX and DTPA-700DX-MB were recorded at 300–800 nm with the Tecan Infinite 200 Pro (Tecan, Männedorf, Switzerland). Emission spectra at 650–800 nm were recorded after 620 nm excitation.

2.2. Radiolabeling with ^{111}In and Quality Control

DTPA-700DX-MB was incubated with 0.4 MBq/ μ g [^{111}In]InCl₃ (Curium, Petten, The Netherlands) for in vitro studies and with 0.042 MBq/ μ g [^{111}In]InCl₃ for in vivo studies and twice the volume of 0.5 M 2-(N-morpholino)ethanesulfonic (MES) buffer, pH 5.5, for 30 min at room temperature. Labelling efficiency and radiochemical purity were determined by instant thin-layer chromatography (ITLC) on a silica-gel chromatography strip (Agilent Technologies, Amstelveen, The Netherlands), using 0.1 M citrate buffer, pH 6.0, as the mobile phase. Furthermore, we determined the purity of the non-conjugated minibody, the conjugate DTPA-700DX-MB, and 0.1 MBq/ μ g ^{111}In -labelled DTPA-700DX-MB with fast protein liquid chromatography (FPLC), using an Agilent Technologies 1260 Infinity with Yarra 3 μ m SEC 3000 column (300 \times 7.8 mm, Phenomenex, Torrance, CA, USA) with 0.1 M sodium phosphate 10% 2-propanol as eluent at a flow rate of 0.7 mL/min.

2.3. Cell Culture

PDAC299 cells (derived from a pancreatic tumour of a Ptf1a^{WT/Cre}; Kras^{WT/LSL-G12D}; P53^{LSL-R172H}/fl mouse [40]) were cultured in DMEM with glutamax (Gibco) supplemented with sodium-pyruvate and 10% FCS at 37 °C in a humidified atmosphere with 5% CO₂. NIH-3T3 fibroblasts and NIH-3T3 fibroblasts stably transfected with murine FAP (3T3-FAP; PETR4906, developed by Roche) were cultured in DMEM with glutamax, supplemented with 10% FCS, penicillin, and streptomycin (and 1.5 μ g/mL puromycin in case of 3T3-FAP) at 37 °C in a humidified atmosphere with 5% CO₂.

2.4. In Vitro Binding and Internalization of DTPA-700DX-MB

3T3, 3T3-FAP, and PDAC299 cells were grown to 80% confluency in 6-well plates and incubated with 1600 Bq ^{111}In -labelled DTPA-700DX-MB in binding buffer (DMEM with 0.5% BSA) at 37 °C for 1, 2.5, or 24 h. After washing twice with PBS, cells were incubated with ice-cold 0.1 M acetic acid and 154 mM NaCl (pH 2.6) for 10 min at 4 °C to collect the membrane-bound fraction. After washing, cells were lysed using 0.1 M NaOH, the lysate was collected, and activity in both fractions was counted in a γ -counter (2480 Wizard 3'', LKB/Wallace, Perkin-Elmer, Boston, MA, USA).

2.5. IC50 Determination

3T3-FAP cells were grown to 90% confluency in 12-well plates. Cells were incubated with increasing concentrations of unlabelled DTPA-700DX-MB (0.015 to 100 nM) in the binding buffer, in the presence of 1600 Bq of ^{111}In -labelled DTPA-700DX-MB for 4 h on ice. Subsequently, cells were washed twice with PBS and lysed using 1 mL 0.1 M NaOH. Activity in the lysates was counted in a γ -counter (2480 Wizard 3'', LKB/Wallace, Perkin-Elmer, Boston, MA, USA). The IC50 values were calculated in Graphpad Prism version 5.0.

2.6. Singlet Oxygen Production

250 nM DTPA-700DX-MB was incubated with 50 μ M p-nitrosodimethylaniline (RNO) and 400 μ M imidazole as an acceptor of singlet oxygen in PBS pH 7.4, in clear, flat-bottom 96-well plates (Costar) and exposed to 690 nm light at 200 mW/cm² with a light emitting diode (LEDfactory, Leeuwarden, The Netherlands) [41]. Absorbance at 440 nm was measured every minute up to 13 min (156 J/cm² total light dose) with the Tecan Infinite[®] 200 Pro (Tecan, Männedorf, Switzerland) to determine singlet oxygen-induced bleaching of RNO.

2.7. *In Vitro Targeted Photodynamic Therapy with DTPA-700DX-MB*

3T3, 3T3-FAP, and PDAC299 cells were grown to 80% confluency in 96-well plates and incubated with DTPA-700DX-MB in binding buffer (DMEM with 0.5% *w/v* BSA, BB) or with BB alone at 37 °C in a humidified atmosphere with 5% CO₂ for 2.5 h. After washing with PBS, regular culture medium was added. The cells were then exposed to 0 or 60 J/cm² 690 nm light at a fluency rate of 200 mW/cm². Cell viability was measured 24 h after tPDT using the CellTiter-Glo assay (Promega, Madison, WI, USA). Furthermore, 3T3-FAP cells were labelled with Vybrant DiO dye according to manufacturer's protocol (Thermo Fisher Scientific, Waltham, MA, USA) and cocultured with PDAC299 tumour cells in Costar 96-well flat-bottom, clear plates in DMEM with 10% FCS. Cells were incubated with 3 nM DTPA-700DX-MB for 2 h at 37 °C, and upon washing, the plate was irradiated with 60 J/cm² 690 nm light. After 24 h, the cells were incubated with 1 µg/mL propidium iodide (PI) in PBS. After washing twice with PBS, cells were imaged with the EVOS FL cell imaging system with the suitable LED cubes (PI = RFP; DiO = GFP).

2.8. *Animals*

The Radboud University animal ethics committee approved study protocols (CCD number AVD1030020209645). All procedures were performed according to the Institute of Laboratory Animal Research guide for Laboratory Animals. All 6–8-week-old female C57BL/6 mice (6JRj, Janvier) were acclimatized for 1 week upon arrival at our institution. They were fed standard chow ad libitum and housed on a 12 h day–night cycle.

Subcutaneous model—Mice were injected subcutaneously at one or both shoulders with 5×10^5 PDAC299 tumour cells resuspended in 100 µL of DMEM. Mice were weighed, and tumours were measured with a calliper twice a week. Tumour size was calculated as follows: tumour size = $(4/3) * \pi * (L/2) * (W/2) * (D/2)$, with L being tumour length, W being tumour width, and D being tumour depth. When (one of the) tumours reached a size of 200 mm³, usually within 10–14 days, animals were included in the experiments.

Orthotopic model—The pancreas was exposed by making a surgical incision just below the spleen. Either 5×10^3 ($n = 5$) or 2.5×10^4 ($n = 4$) PDAC tumour cells resuspended in 30 µL of DMEM and Matrigel (1:1) were injected into the pancreas with a 27G needle. The wound was closed with a surgical suture, and mice were weighed and imaged with ultrasound (Vevo 2100 preclinical imaging system, Visual Sonics, Amsterdam, The Netherlands, MS-550D transducer) twice per week. At 32 days post injection, when the tumours reached a size of 300–500 mm³, mice were included in the experiment.

2.9. *Biodistribution of ¹¹¹In-Labelled DTPA-700DX-MB*

Subcutaneous model—0.3 nmol 10 MBq (for autoradiography analyses and ex vivo biodistribution) or 1 MBq (for ex vivo biodistribution only) ¹¹¹In-labelled DTPA-700DX-MB in 200 µL PBS was injected intravenously in mice carrying PDAC299 subcutaneous tumours. At 4 h ($n = 5$), 24 h ($n = 7$), and 48 h ($n = 5$) post injection, mice were sacrificed through CO₂/O₂ asphyxiation. Three additional mice were co-injected with a 7.4-fold excess non-conjugated and unlabelled minibody and sacrificed at 24 h to determine specificity of uptake. Tumour, blood, and organs were collected, weighed, and counted in a γ -counter (WIZARD, 2480 Automatic Gamma Counter, Perkin-Elmer, Boston, MA, USA). Uptake in the tissues was calculated as the percentage of the injected activity per gram of tissue (%IA/g). Tumours of the mice injected with 10 MBq were processed for autoradiography analyses as described below.

Orthotopic model—0.3 nmol 10 MBq (for autoradiography analyses and ex vivo biodistribution) or 1 MBq (for ex vivo biodistribution only) ¹¹¹In-labelled DTPA-700DX-MB in 200 µL PBS was injected intravenously in mice carrying orthotopic PDAC299 tumours (5×10^3 cells $n = 3$; 2.5×10^4 cells $n = 4$). Two additional mice in the group injected with 5×10^3 tumour cells were co-injected with a 7-fold excess non-conjugated and unlabelled minibody. At 24 h post injection, mice were sacrificed through CO₂/O₂ asphyxiation. Tumour, blood, and organs were collected, weighed, and counted in a γ -counter (WIZARD,

2480 Automatic Gamma Counter, Perkin-Elmer, Boston, MA, USA). Uptake in the tissues was calculated as the percentage of the injected activity per gram of tissue (%IA/g). Tumours of the mice injected with 10 MBq were processed for autoradiography analyses as described below.

2.10. MicroSPECT/CT

A SPECT/CT scan was acquired for 30 min 24 h post injection of one mouse carrying an orthotopic PDAC299 tumour with 10 MBq ^{111}In -labelled DTPA-700DX-MB using a U-SPECT/CT-6 (MILabs, Utrecht, The Netherlands). Images were acquired using a 1 mm diameter pinhole ultra-high-sensitivity mouse collimator. The SPECT scan was reconstructed with three iterations and a voxel size of 0.4 mm (MILabs reconstruction software version 12.00), and the image was made with VivoQuant software (Version 2020R2 build9).

2.11. Autoradiography

Tumours were harvested and formalin-fixed and paraffin-embedded (FFPE). They were cut into 4 μm sections and mounted on superfrost glass slides. A phosphor screen (Fuji Film BAS-IP SR 2025, Raytest, Straubenhardt, Germany) was exposed to the slides for 72 h in a Fujifilm BAS cassette 2025. Then, the images were acquired with a Typhoon FLA 7000 laser scanner (GE healthcare Life Sciences, Chicago, IL, USA) at a pixel size of 25 \times 25 μm . Images were analysed with Aida Image analysis software (Version 4.21, Elysia Raytest, Germany).

2.12. In Vivo FAP-tPDT with DTPA-700DX-MB in the Subcutaneous PDAC299 Model

Mice carrying subcutaneous tumours of PDAC299 on both shoulders were injected with 0.6 nmol DTPA-700DX-MB in PBS ($n = 6$) or PBS alone ($n = 5$). At 24 h post injection, mice were anaesthetized with isoflurane (1.5% in 1 L/min oxygen). Uptake in both tumours was visualized with fluorescence imaging (Excitation filter 640 nm, Emission filter Cy5.5 (IVIS Lumina II, PerkinElmer, Waltham, MA, USA)), and then, one of the tumours was exposed to 50–200 J/cm^2 690 nm light at 230–300 mW/cm^2 (DTPA-700DX-MB group: one dose of 55 J/cm^2 at 280 mW/cm^2 ($n = 1$), three doses of 55 J/cm^2 at 280 mW/cm^2 ($n = 1$), two doses of 100 J/cm^2 at 230 mW/cm^2 ($n = 1$), and one dose of 100 J/cm^2 at 230 mW/cm^2 ($n = 3$); and the PBS group: one dose of 100 J/cm^2 at 230 mW/cm^2 ($n = 5$)). We irradiated the left tumour unless indicated otherwise. The rest of the body was shielded from light using paper towels and aluminium foil. After irradiation, the treated tumour was imaged for fluorescence again. Mice were sacrificed at 24 h post light irradiation with CO_2/O_2 asphyxiation. Tumours, livers, kidneys, and spleens were obtained and formalin-fixed and paraffin-embedded.

2.13. Histology and Immunohistochemistry

FFPE tumours were sectioned at 4 μm thickness. HE and Sirius red staining were performed using standard protocol. Immunohistochemistry (IHC) was performed with rabbit-anti-FAP (EPR20021, ab 207178, Abcam, Cambridge, UK, 1:100 in PBS/1%BSA, binds to both human and murine FAP) and rabbit-anti-cleaved caspase-3 (9661S, Cell signalling technologies, 1:4000 in PBS/1%BSA) antibodies. First, the slides were deparaffinized and rehydrated.

For the FAP staining, antigen retrieval was performed by heating in EDTA for 10 min at 96 $^\circ\text{C}$ in a PT Module (Thermo Fisher Scientific, Waltham, MA, USA). The endogenous peroxidase activity was blocked by incubating with 3% H_2O_2 in PBS for 10 min at room temperature, and endogenous biotin was blocked with a biotin/avidin blocking kit (VECTASTAIN, Thermo fisher) for 15 min at room temperature each. Non-specific binding was blocked through preincubation with 20% normal goat serum for 30 min at room temperature. The slides were subsequently incubated with the primary antibody for 1 h at room temperature and with secondary biotinylated goat-anti-rabbit (VECTASTAIN, 1/200 in PBS 1%/BSA) for 30 min, followed by labelling with the avidin-biotin complex (VECTASTAIN, Thermo Fisher, 1/100). The antibody complex was visualized using 8 min incubation with diaminobenzene (bright DAB, Immunologic, VWR, Dublin, Ireland). All slides were

counterstained with haematoxylin (Klinipath, Olen, Belgium) for 5 s and mounted with a cover slip (Permount, Thermo-Fisher, Waltham, MA, USA).

For the cleaved caspase-3 staining, antigen retrieval was performed by heating in 10 mM citrate, pH 6.0, for 10 min at 96 °C in a PT Module (Thermo Fisher Scientific, Waltham, MA, USA). The peroxidase activity was blocked by incubating with 3% H₂O₂ in PBS. Non-specific binding was blocked through preincubation with 20% normal goat serum for 30 min at room temperature. The slides were subsequently incubated overnight at 4 °C with the primary antibody and with secondary biotinylated goat-anti-rabbit (VECTASTAIN, Thermo Fisher, 1/200 in PBS 1%/BSA) for 30 min, followed by labelling with the avidin-biotin complex (VECTASTAIN, Thermo Fisher, 1/100). The antibody complex was visualized using 8 min incubation with bright DAB. All slides were counterstained with haematoxylin for 5 s and mounted with a Permount cover slip.

2.14. Automated Quantification Cleaved Caspase-3 IHC

Slide digitization was performed using a 3DHistech P1000 scanner digital slide scanner (3DHistech, Budapest, Hungary) with a 20× objective at a resolution of 0.24 µm/pixel. To quantify the amount of cleaved caspase-3 after FAP-tPDT, the total tumour area was manually annotated on tissue sections from two different depths in the tumour (approximately 150 µm apart). Tissue folds and staining artefacts were excluded from the annotation. A previously developed automated colour deconvolution algorithm [42] was used to extract the DAB staining from the background haematoxylin staining. This algorithm automatically determines the optimal stain matrix per slide, which is used for unmixing the slide for an optimal colour unmixing. To achieve this, an adapted version of the deconvolution of Ruifrok et al. was used [43]. We extended this algorithm by computing the ratio (positive pixels for a staining per region of interest) using automated Otsu thresholding on a resolution of 2 µm/pixel, which resulted in a thresholded image. The ratio was calculated on this thresholded image by dividing the stain of interest by the total amount of stained pixels.

2.15. Distribution Visualisation FAP IHC

To compare the autoradiography signal with the FAP IHC staining, we used the same algorithm to analyse the FAP staining. Instead of using the ratio as output, the thresholded image was used. To compare the FAP IHC staining with autoradiography, which are different in terms of resolution, we generated FAP IHC density maps, which mimic the resolution of the autoradiography (25 µm/pixel). A density map was calculated based on the thresholded binary image of the FAP staining. For this purpose, we defined a circular kernel of 0.49 mm² at a resolution of 32 µm/pixel and applied it to the slide in a sliding window fashion, computing the ratio of positive pixels over the circle area for every position in the slide. To limit the analysis to valid pixels in the tumour area within the slide, only positions within the tumour annotations were considered while sliding the circular kernel.

2.16. Statistics

All quantitative data are expressed as mean ± SD. The statistical analyses were performed using GraphPad Prism (Version 5.0, GraphPad Software Inc., San Diego, CA, USA). Student's *t*-test was used to determine significance.

3. Results

3.1. DTPA-700DX-MB Binds to FAP-Expressing Cells and Causes Light-Induced Toxicity

The FAP-binding minibody was conjugated to DTPA-ITC and IRDye700DX-NHS using standardized protocols, reaching a ratio of 1.25 IRDye700DX molecules per minibody (Figure 1A). Though FPLC showed an increase of 5.93% to 14.88% of aggregates upon conjugation (Supplementary Figure S1A,B), spectral properties of the IRDye700DX were retained upon conjugation (Figure 1B). The construct was labelled with ¹¹¹In in 0.5 M MES buffer (pH 5.4) for 20 min, and successful labelling was determined with ITLC and FPLC (Supplementary Figure S1C). Membrane binding of DTPA-700DX-MB to 3T3-FAP cells was

confirmed (3.4 ± 0.07 , 6.7 ± 0.9 , and 11.1 ± 0.13 percentage of added activity at 1, 2.5, and 24 h incubation, respectively), and the construct was efficiently internalized (6.8 ± 0.14 , 11.8 ± 0.41 , and 16.2 ± 0.98 percentage of added activity at 1, 2.5, and 24 h incubation, respectively) (Figure 1C). Lack of binding or internalization in native 3T3 cells as well as in 3T3-FAP cells pre-incubated with an excess unlabelled minibody confirm FAP specificity. The half-maximal inhibitory concentration of DTPA-700DX-MB was 44 nM (Figure 1D). The conjugate produced singlet oxygen upon irradiation with 690 nm light with similar efficiency as the non-conjugated NHS-IRDye700DX (Figure 1E). Upon incubation with varying doses of DTPA-700DX-MB and subsequent irradiation with 60 J/cm^2 200 mW/cm² 690 nm light, efficient cell death was induced (Figure 1F). This effect was not observed when incubating native 3T3 cells or without irradiation, indicating receptor specificity and lack of dark toxicity of DTPA-700DX-MB (Figure 1F). Since on some tumour cell lines expression of FAP is observed, we investigated the binding of DTPA-700DX-MB to PDAC299 cells, but no binding or light-induced cytotoxicity was observed (Supplementary Figure S2A,B). This indicates that these cells do not express FAP, which was also verified in co-cultures of PDAC299 and 3T3-FAP, in which only 3T3-FAP cells were killed upon treatment with DTPA-700DX-MB and light (Supplementary Figure S2C).

3.2. DTPA-700DX-MB Targets Subcutaneous PDAC299 Tumours In Vivo

PDAC299 is a tumour cell line that is derived from the pancreatic tumour of a *Ptfla*^{WT/Cre;Kras}^{WT/LSL-G12D} *P53*^{LSL-R172H/fl} mouse [40]. Upon subcutaneous injection into C57BL/6 mice, these tumours show a moderately well-differentiated morphology organized in glandular structures that are typical for adenocarcinomas (Figure 2A, HE). Furthermore, FAP-expressing fibroblasts were present (Figure 2A, FAP IHC), and excessive collagen formation was found in these tumours (Figure 2A, Sirius red). In a time-optimization biodistribution in mice carrying subcutaneous tumours of PDAC299, a maximum relative tumour uptake of 7.3 ± 1.02 %IA/g and a tumour-to-blood ratio of 8.3 ± 0.82 were observed at 24 h post injection of 0.3 nmol ¹¹¹In-labelled DTPA-700DX-MB (Figure 2B,C and Supplementary Table S1). Tumour uptake was significantly lower upon co-injection of a 7.4x excess of unlabelled and unconjugated minibody (4.4 ± 1.45 %IA/g, $p = 0.0059$), indicating at least a partly FAP-specific uptake (Figure 2B and visualization of IRDye700DX-derived fluorescence in Figure 2D). The main clearance route of DTPA-700DX-MB is the liver, and some uptake was observed in the kidney and spleen. Furthermore, FAP-dependent uptake was observed in the tibia (9.85 ± 1.09 vs. 3.64 ± 0.80 %IA/g upon blocking, $p < 0.0001$), which is most likely due to presence of FAP-expressing cells in the bone marrow. Autoradiography of PDAC299 tumour sections showed heterogenous distribution of DTPA-700DX-MB in the tumour (Figure 2E). To compare the autoradiography signal with the FAP IHC staining, which are different in terms of resolution, we generated FAP IHC density maps, which mimic the resolution of the autoradiography. In general, regions with a high signal on autoradiography also showed a higher signal on FAP IHC density maps visually, while in regions with a low signal on autoradiography, little FAP expression was observed on immunohistochemistry (Figures 2E and S3).

3.3. DTPA-700DX-MB Induces Cell Death in Subcutaneous PDAC299 Tumours In Vivo

To determine in vivo efficacy, mice carrying two PDAC299 tumours were injected with 0.6 nmol DTPA-700DX-MB ($n = 6$) or PBS as a control ($n = 5$). One of the tumours was exposed to 690 nm light. Bleaching of IRDye700DX-derived fluorescence indicated efficient activation of the photosensitizer. A light dose of 55 J/cm^2 at a dose rate of 280 mW/cm^2 was not sufficient to induce apoptosis ($n = 1$, Figure S4). Irradiation with three separate doses of 55 J/cm^2 at 280 mW/cm^2 and two separate doses of 100 J/cm^2 at 230 mW/cm^2 light did induce apoptosis; however, in these conditions, we saw immediate bleeding of the skin and induction of crust formation, most probably due to excessive heating (both $n = 1$, Figure S4). A single dose of 100 J/cm^2 at 230 mW/cm^2 did not result in bleeding or crust formation but did induce apoptosis, as illustrated by the increase in caspase-3-positive

fraction when compared to the contralateral non-irradiated tumours ($n = 3$, 0.41 ± 0.17 vs. 0.01 ± 0.01) (Figures 3A and S5). In the group injected with PBS, some upregulation of apoptosis was observed as well when comparing the caspase-3-positive fraction of the irradiated tumour with the non-irradiated tumour ($n = 5$, 0.23 ± 0.15 vs. 0.029 ± 0.012); however, this effect was less apparent than for the minibody-treated group ($p = 0.0432$ when comparing the MB and PBS light-exposed groups, Figures 3B and S6).

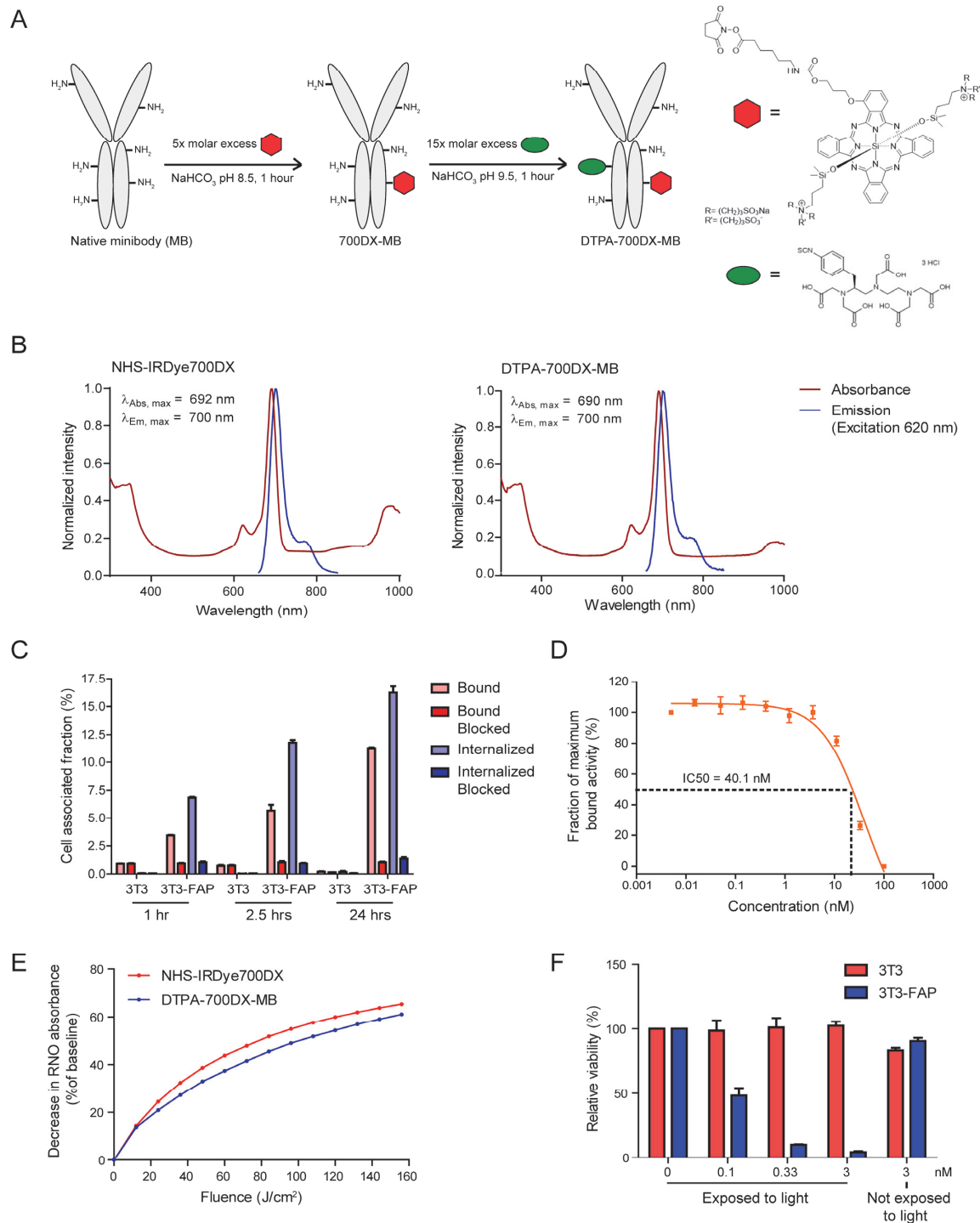


Figure 1. In vitro characterization of DTPA-700DX-MB. (A) Scheme for conjugation of IRDye700DX-NHS and DTPA-ITC to the minibody to generate DTPA-700DX-MB. (B) Normalized photophysical spectra (absorbance and emission at 620 excitation) of 5 μ M NHS-IRDye700DX (left) and 5 μ M DTPA-700DX-MB (right) in PBS. (C) Bound and internalized fractions of 111 In-labelled DTPA-700DX

-MB after 1, 2.5, or 24 h incubation of 3T3 or 3T3-FAP cells at 37 °C. (D) Half-maximal inhibitory concentration. (E) Singlet oxygen production as measured by bleaching of reporter molecule p-nitrosodimethylaniline (RNO). (F) Cell viability of 3T3 and 3T3-FAP cells after incubation of varying doses of DTPA-700DX-MB for 2.5 h and subsequent irradiation with 60 J/cm² 200 mW/cm² 690 nm light. Non-irradiated samples are taken as controls to determine dark toxicity of DTPA-700DX-MB.

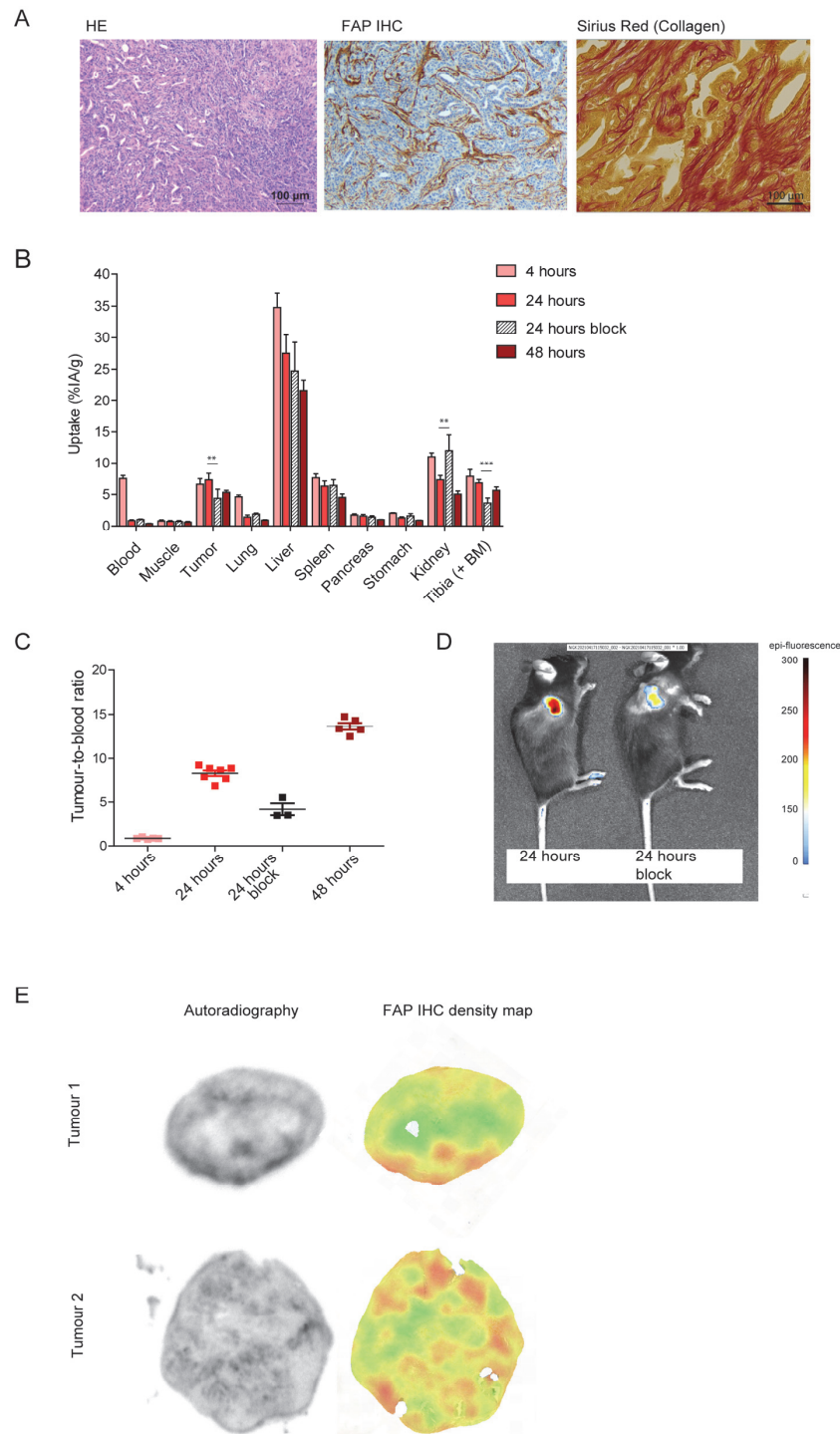


Figure 2. In vivo tumour targeting of DTPA-700DX-MB in subcutaneous PDAC299. (A) Characterization of the PDAC299 model, showing excessive tumour stroma formation and presence of activated fibroblasts, as illustrated by FAP expression and collagen deposition, as shown in the Sirius red staining. (B) In vivo biodistribution depicted as percentage of injected activity dose per gram of tissue at 4, 24, or 48 h after injection of 0.3 nmol 1 MBq ¹¹¹In-labelled DTPA-700DX-MB. One group

of mice was co-injected with a 7.4-fold excess unlabelled minibody. ** $p < 0.01$, *** $p < 0.001$. (C) Tumour-to-blood ratios calculated from the biodistribution data. (D) Fluorescence imaging of two mice at 24 h post injection of 0.3 nmol ^{111}In -labelled DTPA-700DX-MB; one mouse was co-injected with a 7.4-fold excess unlabelled minibody (right). (E) Autoradiography of PDAC299 tumour sections upon injection of 0.3 nmol 10 MBq ^{111}In -labelled DTPA-700DX-MB and FAP IHC density maps, which represent the FAP IHC staining in resolution comparable to the autoradiography.

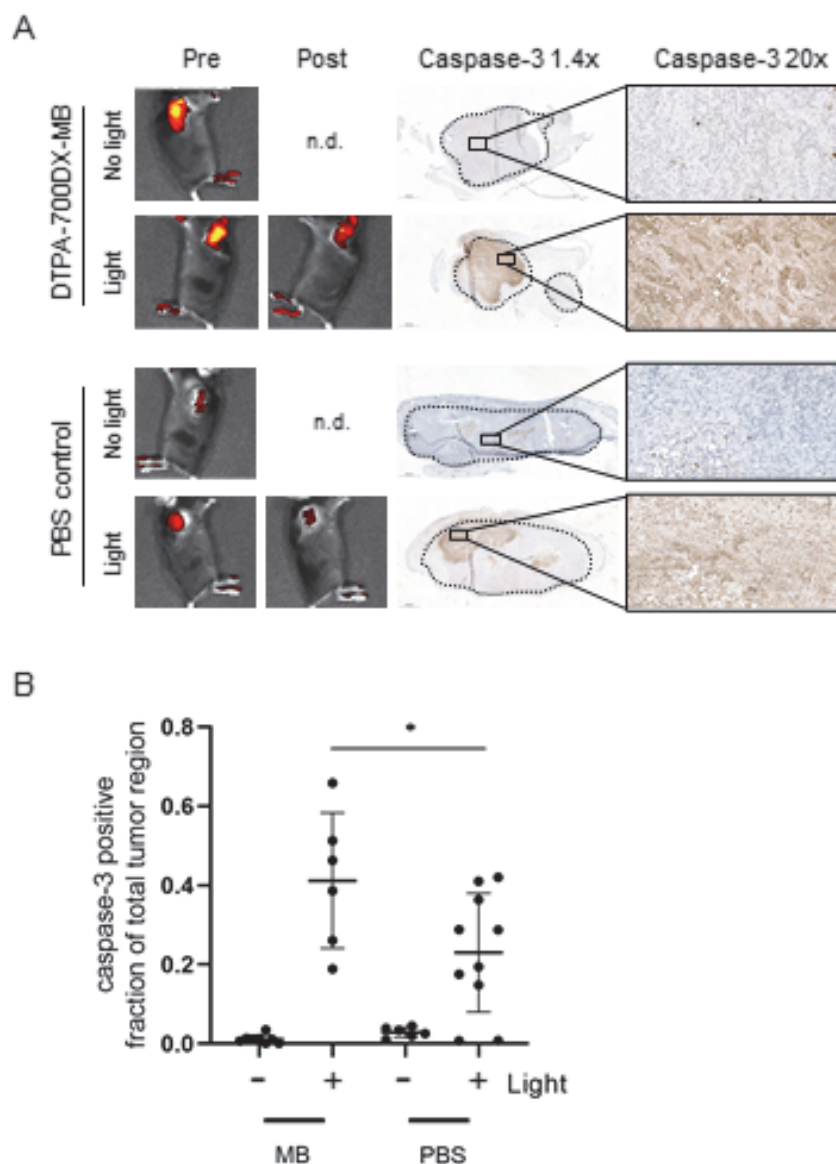


Figure 3. In vivo efficacy of targeted photodynamic therapy with DTPA-700DX-MB in subcutaneous PDAC299. (A) Pictures are representative images from the minibody-treated and the PBS control groups. Mice carrying subcutaneous PDAC299 tumours were injected with 0.6 nmol DTPA-700DX-MB 24 h after injection fluorescence was visualized (pre), then tumours were exposed to 100 J/cm² 230 mW/cm² of 690 nm light, and fluorescence was visualized again (post). Tumours were formalin-fixed and paraffin-embedded, and induction of apoptosis was assessed with IHC. (B) Automated quantification of the percentage caspase-3-positive region of the whole tumour region, for two sections per tumour. * $p < 0.05$.

3.4. DTPA-700DX-MB Targets PDAC299 Orthotopic Tumours In Vivo

Maximum relative tumour uptakes of 8.97 ± 2.01 %IA/g and 9.28 ± 1.44 %IA/g were observed at 24 h post injection of 0.3 nmol ^{111}In -labelled DTPA-700DX-MB in mice injected with 5×10^3 and 2.5×10^4 tumour cells, respectively (Figure 4A and Table S2). Tumour

uptake was 7.89 ± 2.03 %IA/g upon co-injection of a 7-fold excess of unlabelled and un-conjugated minibody (not significant). As in the mice carrying subcutaneous tumours, we observed uptake in the liver, kidney, and spleen. Furthermore, FAP-dependent uptake was observed in the tibia (6.61 ± 0.55 vs. 4.15 ± 0.12 %IA/g upon blocking, $p = 0.0096$). The signal in the orthotopic tumour could be visualized with SPECT/CT imaging (Figure 4B, tumour area is encircled). Autoradiography of PDAC299 tumour sections showed heterogeneous distribution of DTPA-700DX-MB. Similar to the subcutaneous tumours, comparable patterns were observed for the autoradiography and FAP-IHC density maps in the orthotopic tumours (Figures 4C and S7).

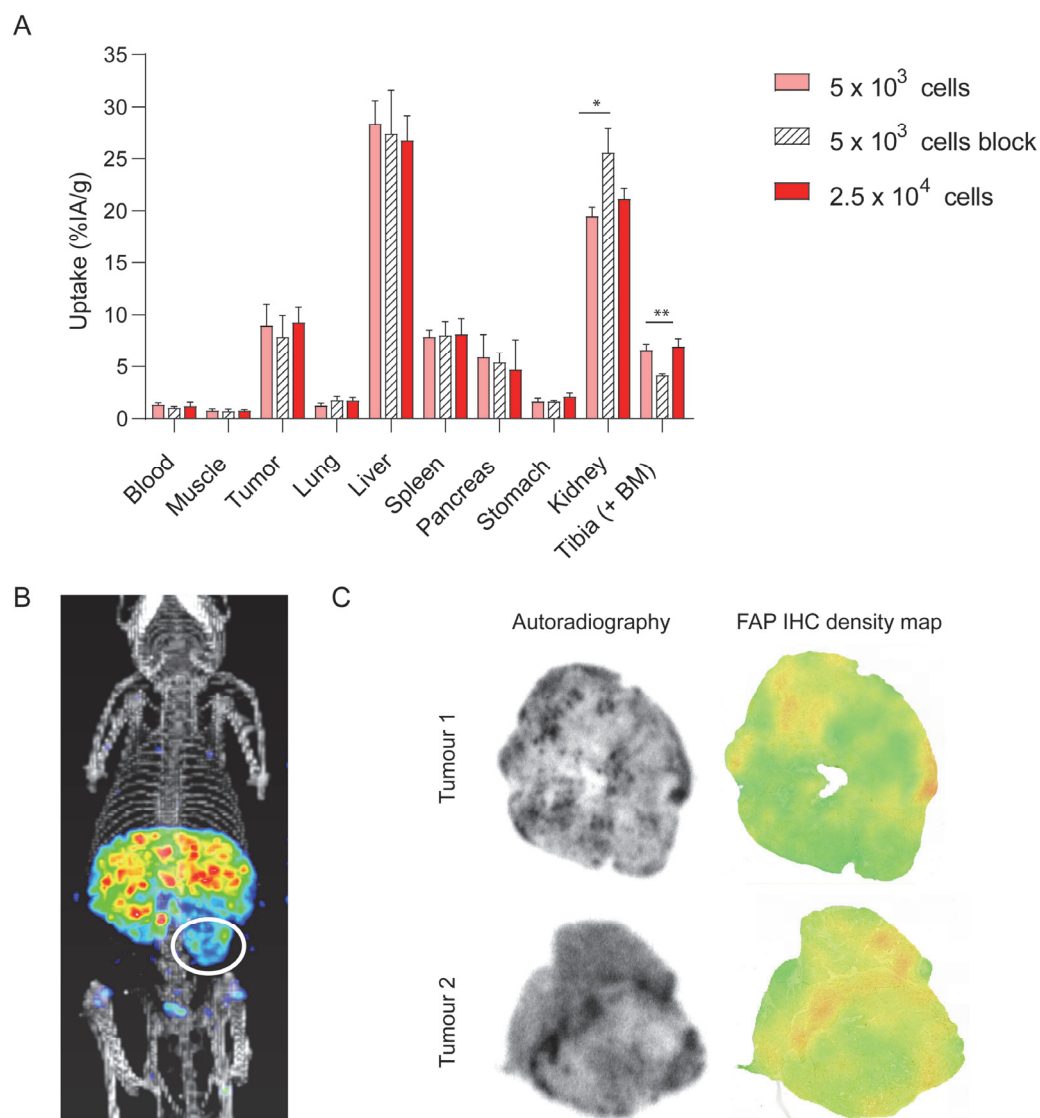


Figure 4. In vivo tumour targeting of DTPA-700DX-MB in an orthotopic model. (A) In vivo biodistribution depicted as percentage of injected activity dose per gram of tissue at 24 h after injection of 0.3 nmol 10 MBq ^{111}In -labelled DTPA-700DX-MB in mice carrying orthotopic PDAC299 tumours. Two mice were co-injected with a 7-fold excess unlabelled minibody. * $p < 0.05$, ** $p < 0.01$. (B) Micro-SPECT/CT imaging of a mouse at 24 h post injection of 0.3 nmol 10 MBq ^{111}In -labelled DTPA-700DX-MB. (C) Autoradiography of orthotopic PDAC299 tumour sections upon injection of 0.3 nmol 10 MBq ^{111}In -labelled DTPA-700DX-MB and FAP IHC density maps, which represent the FAP IHC staining in resolution comparable to the autoradiography.

4. Discussion

FAP-expressing CAFs are shown to have pro-tumourigenic effects in multiple solid tumour types. In this work, we characterize DTPA-700DX-MB, which can be used for light-induced ablation of FAP-expressing cells.

The anti-FAP minibody was efficiently functionalized with the photosensitizer IRDye700DX, which is one of the most suitable photosensitizers for targeted photodynamic therapy due to its high hydrophilicity, photostability, and singlet oxygen quantum yield [22]. We demonstrated efficient and specific binding to murine FAP-transfected 3T3 fibroblasts and toxicity upon exposure to 690 nm light. *In vivo*, we showed targeting to both subcutaneous and orthotopic PDAC299 tumours. The uptake is at least partly specific, as shown by inhibition of accumulation after administration of an excess unlabelled minibody and colocalization of the minibody with FAP expression, as determined immunohistochemically. The limited molar excess of minibody (7-fold as compared to up to 100-fold used in other blocking studies) could lead to an underestimation of FAP-specific uptake. In the *in vivo* therapy experiment, we observed induction of apoptosis in the PDAC299 subcutaneous tumours, as illustrated by cleaved caspase-3 expression, in both the minibody and PBS-treated groups following light exposure. The upregulation in the minibody-treated group was, however, more pronounced, and part of the upregulation of caspase-3 expression may have been induced by excessive heating [44]. Surprisingly, we also observed a low auto-fluorescent signal in the tumours of PBS-injected mice, which was bleached upon irradiation. Though the origin of this fluorescent signal is unknown and has not been described in other studies, this may also be another contributor to the increase of caspase-3 staining that we observed in these tumours.

In these studies, we used a syngeneic mouse model PDAC299 using a murine cell line with PDAC typical KRAS and Trp53 mutations. We have shown that the subcutaneous PDAC299 tumours have an abundant stroma with collagen bundles containing FAP-expressing fibroblasts. As this model shows physiological overexpression of FAP on the stromal component, as is seen in human tumours as well, we believe that it better recapitulates the physiological situation as opposed to models that have been used in other studies, such as mixtures of cancer cells and fibroblasts and human tumour cell lines with either physiological or artificial FAP overexpression. Though the subcutaneous model is adequate to provide insight into pharmacokinetics and targeting properties of the DTPA-700DX-MB, we do believe that further studies into the biological effects of the FAP-targeted PDT should be investigated in orthotopic models because those better reflect the local environment in which the tumours develop.

Other groups have employed FAP-targeted PDT with a nanoparticle and an antibody [26,30–33]. Zhen et al. showed efficient killing of fibroblasts in the murine breast cancer model 4T1, which resulted in increased CD8⁺ T-cell infiltration. Katsube et al. reported efficient killing of CAFs in a murine model that was co-inoculated with human squamous carcinoma cells (TE4) and activated human foetal oesophageal fibroblasts (FEF3), which improved the sensitivity to conventional chemotherapy. These results indicate the potential therapeutic efficacy of FAP-targeted photodynamic therapy in multiple tumour types. As mentioned above, further studies in an orthotopic PDAC299 model with varying light and protein doses are needed to determine the effect on immunomodulation and efficacy of other systemic therapies such as chemo- and immunotherapies.

Besides FAP-targeted PDT, radionuclide therapy with FAP-targeting small molecules has gained attention over the past years. FAP-targeting small molecules labelled with actinium-226 or lutetium-177 showed modest growth inhibition in preclinical studies, and initial clinical studies are emerging [45–47]. Though systemic toxicities are a potential problem of radionuclide therapies, an advantage is that the therapeutic effect occurs in all lesions in the body, and it is thus suitable for application in metastasized disease. PDT can only be used for tumours that are accessible to light that has a limited penetration depth (up to 1 cm for NIR light). We therefore envision clinical application of FAP-tPDT to be applied intraoperatively or through multiple laser fibres for larger and more deeper-seated lesions of localized disease.

Furthermore, we expect this therapy to be applied in an adjuvant manner, sensitizing the tumours for other systemic therapies such as chemotherapy and immunotherapy.

5. Conclusions

In conclusion, we have shown that the DTPA-700DX-MB conjugate efficiently binds to FAP-expressing cells and induces cell death upon light exposure in vitro. Furthermore, it targets FAP-expressing fibroblasts in PDAC299 subcutaneous and orthotopic tumours and induces apoptosis in the subcutaneous tumours upon light exposure. This study provides proof-of-concept of FAP-targeted PDT in PDAC, and future studies should demonstrate the feasibility in other tumour types and the effects on tumour growth, immunomodulation, and efficacy of other systemic therapies.

Supplementary Materials: The following supporting information can be downloaded at: <https://www.mdpi.com/article/10.3390/cells12101420/s1>, Figure S1: FPLC data of the native minibody, DTPA-MB-700DX and ¹¹¹In-labeled DTPA-MB-700DX; Figure S2: Lack of association of DTPA-700DX-MB with PDAC299 cells in vitro, Figure S3: Autoradiography of subcutaneous PDAC299 tumour sections, Figure S4: In vivo efficacy of targeted photodynamic therapy with DTPA-700DX-MB, Figure S5: In vivo efficacy of targeted photodynamic therapy with DTPA-700DX-MB, Figure S6: PBS control group for FAP-targeted photodynamic therapy in vivo, Figure S7: Autoradiography of orthotopic PDAC299 tumour sections, Table S1: Uptake in various tissues in the subcutaneous model, Table S2: Uptake in various tissues in the orthotopic model.

Author Contributions: A.M. and S.A.M.v.L. designed the study; D.N.D., E.M.M.S., G.M.F., M.S.v.E., C.F. and S.A.M.v.L. performed the experiments; M.T.-A. and P.F.C. set up the animal models; S.A.M.v.L. wrote the concept manuscript. All authors including M.W.J.S., J.T.S., I.W. and E.H.J.G.A. revised the manuscript. All authors have read and agreed to the published version of the manuscript.

Funding: This work was financially supported by a Junior Researcher grant from the Radboud Institute for Molecular Life Sciences (RIMLS) and a grant from the Radboud Oncologie Fonds (ROF) and Stichting Bergh in het Zadel, partner of Dutch Cancer Society (KUN2015-8106).

Institutional Review Board Statement: The animal study protocol was approved by the Institutional Review Board (or Ethics Committee) of The Radboud University animal ethics committee (CCD number AVD103002015209 and AVD1030020209645).

Data Availability Statement: The datasets used and/or analysed during the current study are available from the corresponding author on reasonable request.

Acknowledgments: The authors thank Bianca Lemmers-van de Weem, Kitty Lemmens-Hermans, Karin de Haas-Cremers and Floor Moonen from the Central Animal Facility of the Radboud UMC for their expertise and technical assistance with the animal experiments.

Conflicts of Interest: J.T.S. receives honoraria as consultant or for continuing medical education presentations from AstraZeneca, Bayer, Bristol-Myers Squibb, Immunocore, Novartis, Roche/Genentech, and Servier. His institution receives research funding from Bristol-Myers Squibb, Celgene, Eisbach Bio, and Roche/Genentech; he holds ownership and serves on the Board of Directors of Pharma15, all outside the submitted work. A.M. and I.W. are Director of Research and Chief Executive Officer of ImaginAb Inc., respectively.

References

1. Kelly, T.; Huang, Y.; Simms, A.E.; Mazur, A. Fibroblast activation protein-alpha: A key modulator of the microenvironment in multiple pathologies. *Int. Rev. Cell Mol. Biol.* **2012**, *297*, 83–116.
2. Cohen, S.J.; Alpaugh, R.K.; Palazzo, I.; Meropol, N.J.; Rogatko, A.; Xu, Z.; Hoffman, J.P.; Weiner, L.M.; Cheng, J.D. Fibroblast Activation Protein and Its Relationship to Clinical Outcome in Pancreatic Adenocarcinoma. *Pancreas* **2008**, *37*, 154–158. [[CrossRef](#)] [[PubMed](#)]
3. Shi, M.; Yu, D.-H.; Chen, Y.; Zhao, C.-Y.; Zhang, J.; Liu, Q.-H.; Ni, C.-R.; Zhu, M.-H. Expression of fibroblast activation protein in human pancreatic adenocarcinoma and its clinicopathological significance. *World J. Gastroenterol.* **2012**, *18*, 840–846. [[CrossRef](#)] [[PubMed](#)]
4. Lee, H.O.; Mullins, S.R.; Franco-Barraza, J.; Valianou, M.; Cukierman, E.; Cheng, J.D. FAP-overexpressing fibroblasts produce an extracellular matrix that enhances invasive velocity and directionality of pancreatic cancer cells. *BMC Cancer* **2011**, *11*, 245. [[CrossRef](#)]
5. Kraman, M.; Bambrough, P.J.; Arnold, J.N.; Roberts, E.W.; Magiera, L.; Jones, J.O.; Gopinathan, A.; Tuveson, D.A.; Fearon, D.T. Suppression of antitumor immunity by stromal cells expressing fibroblast activation protein-alpha. *Science* **2010**, *330*, 827–830. [[CrossRef](#)]

6. Altmann, A.; Haberkorn, U.A.; Siveke, J. The Latest Developments in Imaging of Fibroblast Activation Protein. *J. Nucl. Med.* **2020**, *62*, 160–167. [[CrossRef](#)] [[PubMed](#)]
7. Imlimthan, S.; Moon, E.S.; Rathke, H.; Afshar-Oromieh, A.; Rösch, F.; Rominger, A.; Gourni, E. New Frontiers in Cancer Imaging and Therapy Based on Radiolabeled Fibroblast Activation Protein Inhibitors: A Rational Review and Current Progress. *Pharmaceuticals* **2021**, *14*, 1023. [[CrossRef](#)]
8. Santos, A.M.; Jung, J.; Aziz, N.; Kissil, J.L.; Puré, E. Targeting fibroblast activation protein inhibits tumor stromagenesis and growth in mice. *J. Clin. Investig.* **2009**, *119*, 3613–3625. [[CrossRef](#)]
9. Lee, J.; Fassnacht, M.; Nair, S.; Boczkowski, D.; Gilboa, E. Tumor Immunotherapy Targeting Fibroblast Activation Protein, a Product Expressed in Tumor-Associated Fibroblasts. *Cancer Res.* **2005**, *65*, 11156–11163. [[CrossRef](#)]
10. Wen, Y.; Wang, C.-T.; Ma, T.-T.; Li, Z.-Y.; Zhou, L.-N.; Mu, B.; Leng, F.; Shi, H.-S.; Li, Y.-O.; Wei, Y.-Q. Immunotherapy targeting fibroblast activation protein inhibits tumor growth and increases survival in a murine colon cancer model. *Cancer Sci.* **2010**, *101*, 2325–2332. [[CrossRef](#)]
11. Loeffler, M.; Krüger, J.A.; Niethammer, A.G.; Reisfeld, R.A. Targeting tumor-associated fibroblasts improves cancer chemotherapy by increasing intratumoral drug uptake. *J. Clin. Investig.* **2006**, *116*, 1955–1962. [[CrossRef](#)] [[PubMed](#)]
12. Wang, L.C.; Lo, A.; Scholler, J.; Sun, J.; Majumdar, R.S.; Kapoor, V.; Antzis, M.; Cotner, C.E.; Johnson, L.A.; Durham, A.C.; et al. Targeting fibroblast activation protein in tumor stroma with chimeric antigen receptor T cells can inhibit tumor growth and augment host immunity without severe toxicity. *Cancer Immunol. Res.* **2014**, *2*, 154–166. [[CrossRef](#)]
13. Watabe, T.; Liu, Y.; Kaneda-Nakashima, K.; Shirakami, Y.; Lindner, T.; Ooe, K.; Toyoshima, A.; Nagata, K.; Shimosegawa, E.; Haberkorn, U.; et al. Theranostics Targeting Fibroblast Activation Protein in the Tumor Stroma: 64Cu- and 225Ac-Labeled FAPI-04 in Pancreatic Cancer Xenograft Mouse Models. *J. Nucl. Med.* **2020**, *61*, 563–569. [[CrossRef](#)] [[PubMed](#)]
14. Kim, M.-G.; Shon, Y.; Kim, J.; Oh, Y.-K. Selective Activation of Anticancer Chemotherapy by Cancer-Associated Fibroblasts in the Tumor Microenvironment. *J. Natl. Cancer Inst.* **2017**, *109*, djw186. [[CrossRef](#)] [[PubMed](#)]
15. LeBeau, A.M.; Brennen, W.N.; Aggarwal, S.; Denmeade, S.R. Targeting the cancer stroma with a fibroblast activation protein-activated promelittin protoxin. *Mol. Cancer Ther.* **2009**, *8*, 1378–1386. [[CrossRef](#)]
16. Roy, J.; Hettiarachchi, S.U.; Kaake, M.; Mukkamala, R.; Low, P.S. Design and validation of fibroblast activation protein alpha targeted imaging and therapeutic agents. *Theranostics* **2020**, *10*, 5778–5789. [[CrossRef](#)]
17. Fischer, E.; Chaitanya, K.; Wuest, T.; Wadle, A.; Scott, A.M.; van den Broek, M.; Schibli, R.; Bauer, S.; Renner, C. Radioimmunotherapy of fibroblast activation protein positive tumors by rapidly internalizing antibodies. *Clin. Cancer Res.* **2012**, *18*, 6208–6218. [[CrossRef](#)]
18. Tran, E.; Chinnasamy, D.; Yu, Z.; Morgan, R.A.; Lee, C.-C.R.; Restifo, N.P.; Rosenberg, S.A. Immune targeting of fibroblast activation protein triggers recognition of multipotent bone marrow stromal cells and cachexia. *J. Exp. Med.* **2013**, *210*, 1125–1135. [[CrossRef](#)]
19. Roberts, E.W.; Deonaraine, A.; Jones, J.O.; Denton, A.E.; Feig, C.; Lyons, S.K.; Espeli, M.; Kraman, M.; McKenna, B.; Wells, R.J.B.; et al. Depletion of stromal cells expressing fibroblast activation protein-alpha from skeletal muscle and bone marrow results in cachexia and anemia. *J. Exp. Med.* **2013**, *210*, 1137–1151. [[CrossRef](#)]
20. Dolznig, H.; Schweifer, N.; Puri, C.; Kraut, N.; Rettig, W.J.; Kerjaschki, D.; Garin-Chesa, P. Characterization of cancer stroma markers: In silico analysis of an mRNA expression database for fibroblast activation protein and endosialin. *Cancer Immun.* **2005**, *5*, 10.
21. Niedermeyer, J.; Garin-Chesa, P.; Kriz, M.; Hilberg, F.; Mueller, E.; Bamberger, U.; Schnapp, A. Expression of the fibroblast activation protein during mouse embryo development. *Int. J. Dev. Biol.* **2001**, *45*, 445–447.
22. Mitsunaga, M.; Ogawa, M.; Kosaka, N.; Rosenblum, L.T.; Choyke, P.L.; Kobayashi, H. Cancer cell-selective in vivo near infrared photoimmunotherapy targeting specific membrane molecules. *Nat. Med.* **2011**, *17*, 1685–1691. [[CrossRef](#)] [[PubMed](#)]
23. Kishimoto, S.; Bernardo, M.; Saito, K.; Koyasu, S.; Mitchell, J.B.; Choyke, P.L.; Krishna, M.C. Evaluation of oxygen dependence on in vitro and in vivo cytotoxicity of photoimmunotherapy using IR-700-antibody conjugates. *Free Radic. Biol. Med.* **2015**, *85*, 24–32. [[CrossRef](#)] [[PubMed](#)]
24. Peng, X.; Draney, D.R.; Volcheck, W.M.; Bashford, G.R.; Lamb, D.T.; Grone, D.L.; Zhang, Y.; Johnson, C.M. Phthalocyanine dye as an extremely photostable and highly fluorescent near-infrared labeling reagent. *Opt. Mol. Probes Biomed. Appl.* **2006**, *6097*, 113–124. [[CrossRef](#)]
25. Smeets, E.; Dorst, D.; van Lith, S.; Freimoser-Grundschober, A.; Klein, C.; Trajkovic-Arsic, M.; Gotthardt, M.; Siveke, J.; Aarntzen, E. A dual-labeled anti-FAP antibody for imaging and targeted photodynamic therapy of cancer associated fibroblasts in a pancreatic cancer mouse model. *Eur. J. Nucl. Med. Mol. I* **2019**, *46* (Suppl. S1), S665–S666.
26. Katsube, R.; Noma, K.; Ohara, T.; Nishiwaki, N.; Kobayashi, T.; Komoto, S.; Sato, H.; Kashima, H.; Kato, T.; Kikuchi, S.; et al. Fibroblast activation protein targeted near infrared photoimmunotherapy (NIR PIT) overcomes therapeutic resistance in human esophageal cancer. *Sci. Rep.* **2021**, *11*, 1693. [[CrossRef](#)]
27. Watanabe, S.; Noma, K.; Ohara, T.; Kashima, H.; Sato, H.; Kato, T.; Urano, S.; Katsube, R.; Hashimoto, Y.; Tazawa, H.; et al. Photoimmunotherapy for cancer-associated fibroblasts targeting fibroblast activation protein in human esophageal squamous cell carcinoma. *Cancer Biol. Ther.* **2019**, *20*, 1234–1248. [[CrossRef](#)]

28. Dorst, D.N.; van Caam, A.P.M.; Vitters, E.L.; Walgreen, B.; Helsen, M.M.A.; Klein, C.; Gudi, S.; Wubs, T.; Kumari, J.; Vonk, M.C.; et al. Fibroblast Activation Protein Targeted Photodynamic Therapy Selectively Kills Activated Skin Fibroblasts from Systemic Sclerosis Patients and Prevents Tissue Contraction. *Int. J. Mol. Sci.* **2021**, *22*, 12681. [[CrossRef](#)]
29. Dorst, D.N.; Rijpkema, M.; Buitinga, M.; Walgreen, B.; Helsen, M.M.A.; Brennan, E.; Klein, C.; Laverman, P.; Ramming, A.; Schmidkonz, C.; et al. Targeting of fibroblast activation protein in rheumatoid arthritis patients: Imaging and ex vivo photodynamic therapy. *Rheumatology* **2021**, *61*, 2999–3009. [[CrossRef](#)]
30. Jin, J.; Barnett, J.D.; Krishnamachary, B.; Mironchik, Y.; Luo, C.K.; Kobayashi, H.; Bhujwalla, Z.M. Evaluating near-infrared photoimmunotherapy for targeting fibroblast activation protein- α expressing cells in vitro and in vivo. *Cancer Sci.* **2022**, *114*, 236–246. [[CrossRef](#)]
31. Sato, H.; Noma, K.; Ohara, T.; Kawasaki, K.; Akai, M.; Kobayashi, T.; Nishiwaki, N.; Narusaka, T.; Komoto, S.; Kashima, H.; et al. Dual-targeted near-infrared photoimmunotherapy for esophageal cancer and cancer-associated fibroblasts in the tumor microenvironment. *Sci. Rep.* **2022**, *12*, 20152. [[CrossRef](#)] [[PubMed](#)]
32. Zhou, S.; Zhen, Z.; Paschall, A.V.; Xue, L.; Yang, X.; Blackwell, A.B.; Cao, Z.; Zhang, W.; Wang, M.; Teng, Y.; et al. FAP-Targeted Photodynamic Therapy Mediated by Ferritin Nanoparticles Elicits an Immune Response against Cancer Cells and Cancer Associated Fibroblasts. *Adv. Funct. Mater.* **2020**, *31*, 2007017. [[CrossRef](#)]
33. Zhen, Z.; Tang, W.; Wang, M.; Zhou, S.; Wang, H.; Wu, Z.; Hao, Z.; Li, Z.; Liu, L.; Xie, J. Protein Nanocage Mediated Fibroblast-Activation Protein Targeted Photoimmunotherapy to Enhance Cytotoxic T Cell Infiltration and Tumor Control. *Nano Lett.* **2017**, *17*, 862–869. [[CrossRef](#)] [[PubMed](#)]
34. Watanabe, R.; Hanaoka, H.; Sato, K.; Nagaya, T.; Harada, T.; Mitsunaga, M.; Kim, I.; Paik, C.H.; Wu, A.M.; Choyke, P.L.; et al. Photoimmunotherapy targeting prostate-specific membrane antigen: Are antibody fragments as effective as antibodies? *J. Nucl. Med.* **2015**, *56*, 140–144. [[CrossRef](#)]
35. Van Driel, P.B.; Boonstra, M.C.; Slooter, M.D.; Heukers, R.; Stammes, M.A.; Snoeks, T.J.A.; De Bruijn, H.S.; Van Diest, P.J.; Vahrmeijer, A.L.; van Bergen en Henegouwen, P.M.P.; et al. EGFR targeted nanobody–photosensitizer conjugates for photodynamic therapy in a pre-clinical model of head and neck cancer. *J. Control. Release* **2016**, *229*, 93–105. [[CrossRef](#)]
36. Maresca, K.P.; Chen, J.; Mathur, D.; Giddabasappa, A.; Root, A.; Narula, J.; King, L.; Schaer, D.; Golas, J.; Kobylarz, K.; et al. Preclinical Evaluation of ^{89}Zr -Df-IAB22M2C PET as an Imaging Biomarker for the Development of the GUCY2C-CD3 Bispecific PF-07062119 as a T Cell Engaging Therapy. *Mol. Imaging Biol.* **2021**, *23*, 941–951. [[CrossRef](#)] [[PubMed](#)]
37. Nagle, V.L.; Henry, K.E.; Hertz, C.A.J.; Graham, M.S.; Campos, C.; Parada, L.F.; Pandit-Taskar, N.; Schietinger, A.; Mellinghoff, I.K.; Lewis, J.S. Imaging Tumor-Infiltrating Lymphocytes in Brain Tumors with [(64)Cu]Cu-NOTA-anti-CD8 PET. *Clin. Cancer Res.* **2021**, *27*, 1958–1966. [[CrossRef](#)] [[PubMed](#)]
38. Pandit-Taskar, N.; Postow, M.A.; Hellmann, M.D.; Harding, J.J.; Barker, C.A.; O’Donoghue, J.A.; Ziolkowska, M.; Ruan, S.; Lyashchenko, S.K.; Tsai, F.; et al. First-in-Humans Imaging with (89)Zr-Df-IAB22M2C Anti-CD8 Minibody in Patients with Solid Malignancies: Preliminary Pharmacokinetics, Biodistribution, and Lesion Targeting. *J. Nucl. Med.* **2020**, *61*, 512–519. [[CrossRef](#)]
39. Farwell, M.D.; Gamache, R.F.; Babazada, H.; Hellmann, M.D.; Harding, J.J.; Korn, R.; Mascioni, A.; Le, W.; Wilson, I.; Gordon, M.S.; et al. CD8-targeted PET Imaging of Tumor Infiltrating T cells in Patients with Cancer: A Phase I First-in-Human Study of (89)Zr-Df-IAB22M2C, a Radiolabeled anti-CD8 Minibody. *J. Nucl. Med.* **2021**, *63*, 720–726. [[CrossRef](#)]
40. Hingorani, S.R.; Wang, L.; Multani, A.S.; Combs, C.; Deramaudt, T.B.; Hruban, R.H.; Rustgi, A.K.; Chang, S.; Tuveson, D.A. Trp53R172H and KrasG12D cooperate to promote chromosomal instability and widely metastatic pancreatic ductal adenocarcinoma in mice. *Cancer Cell* **2005**, *7*, 469–483. [[CrossRef](#)]
41. de Boer, E.; Warram, J.M.; Hartmans, E.; Bremer, P.J.; Bijl, B.; Crane, L.M.; Nagengast, W.B.; Rosenthal, E.L.; van Dam, G.M. A Standardized Light-Emitting Diode Device for Photoimmunotherapy. *J. Nucl. Med.* **2014**, *55*, 1893–1898. [[CrossRef](#)] [[PubMed](#)]
42. Geijs, D.J.; Intezar, M.; Litjens, G.J.S.; van der Laak, J.A.W.M. Automatic color unmixing of IHC stained whole slide images. In *Medical Imaging 2018: Digital Pathology*; SPIE: Bellingham, WA USA, 2018; Volume 10581, pp. 165–171. [[CrossRef](#)]
43. Ruifrok, A.C.; Johnston, D.A. Quantification of histochemical staining by color deconvolution. *Anal. Quant. Cytol. Histol.* **2001**, *23*, 291–299.
44. Okuyama, S.; Nagaya, T.; Ogata, F.; Maruoka, Y.; Sato, K.; Nakamura, Y.; Choyke, P.L.; Kobayashi, H. Avoiding thermal injury during near-infrared photoimmunotherapy (NIR-PIT): The importance of NIR light power density. *Oncotarget* **2017**, *8*, 113194–113201. [[CrossRef](#)]
45. Fu, H.M.; Huang, J.; Sun, L.M.; Wu, H.M.; Chen, H.M. FAP-Targeted Radionuclide Therapy of Advanced Radioiodine-Refractory Differentiated Thyroid Cancer with Multiple Cycles of ^{177}Lu -FAP-46. *Clin. Nucl. Med.* **2022**, *47*, 906–907. [[CrossRef](#)] [[PubMed](#)]
46. Fu, K.; Pang, Y.; Zhao, L.; Lin, L.; Wu, H.; Sun, L.; Lin, Q.; Chen, H. FAP-targeted radionuclide therapy with [^{177}Lu]Lu-FAP-46 in metastatic nasopharyngeal carcinoma. *Eur. J. Nucl. Med.* **2021**, *49*, 1767–1769. [[CrossRef](#)] [[PubMed](#)]
47. Baum, R.P.; Schuchardt, C.; Singh, A.; Chantadisai, M.; Robiller, F.C.; Zhang, J.; Mueller, D.; Eismant, A.; Almaguel, F.; Zboralski, D.; et al. Feasibility, Biodistribution, and Preliminary Dosimetry in Peptide-Targeted Radionuclide Therapy of Diverse Adenocarcinomas Using (^{177}Lu)-FAP-2286: First-in-Humans Results. *J. Nucl. Med.* **2022**, *63*, 415–423. [[CrossRef](#)]

Disclaimer/Publisher’s Note: The statements, opinions and data contained in all publications are solely those of the individual author(s) and contributor(s) and not of MDPI and/or the editor(s). MDPI and/or the editor(s) disclaim responsibility for any injury to people or property resulting from any ideas, methods, instructions or products referred to in the content.